Int. J. Electrochem. Sci., 16 **(2021)** Article ID: 210425, doi: 10.20964/2021.04.06

International Journal of
ELECTROCHEMICAL
SCIENCE
www.electrochemsci.org

The Different Roles of Ni^{2+}/Ni^{3+}, Ni^{3+}/Ni^{4+}, and Mn^{3+}/Mn^{4+} in Li-rich Layered Nanostructured $LiNi_xMn_{1-x}O_2{\cdot}Li_2MnO_3$ with High Capacity

Juan Wang[1, 2], *Yu Li*[1, 2], *Rui Liu*[2], *Xiao-Ming Xu*[1], *Cui-Song Zeng*[1], *Xiang-Bo Shen*[1], *Yi-Jie Gu*[1, 2,*]

[1] School of Mechanical-electronic and Vehicle Engineering, Weifang University, Weifang, 261061, China
[2] College of Materials Science and Engineering, Shandong University of Science and Technology, Qingdao 266510, China
[*]E-mail: guyijie@sdust.edu.cn

Received: 11 November 2020 / *Accepted:* 25 January 2021 / *Published:* 28 February 2021

We prepared $LiNi_xMn_{1-x}O_2{\cdot}Li_2MnO_3$ (x = 0.6, 0.7, 0.8, 0.9, 1) Li-rich layered nanostructured cathode materials without Co by co-precipitation, and studied the effects of Ni^{2+}/Ni^{3+}, Ni^{3+}/Ni^{4+}, and Mn^{3+}/Mn^{4+} on their electrochemical properties. The change trend of discharge capacity for $LiNi_xMn_{1-x}O_2{\cdot}Li_2MnO_3$ was influenced by the change trend of the capacity provided by the reduction processes of Ni^{2+}/Ni^{3+}, Ni^{3+}/Ni^{4+}, and Mn^{3+}/Mn^{4+}. Analysis shows that the capacity from nickel is closely related to the content of divalent nickel. As the content of divalent nickel increases, the capacity increases. Compared with divalent nickel, the capacity provided by trivalent nickel basically does not change with the nickel content increasing. The capacity from manganese is affected by the manganese content and the nickel in Li_2MnO_3.

Keywords: Lithium-rich layered materials, Cathode materials, Electrochemical performance

1. INTRODUCTION

Lithium-ion batteries, which operate by relying on the migration of lithium ions between the anode and cathode and its Li ions through intercalation and deintercalation between the two electrodes during charge–discharge, are a type of secondary batteries that are indispensable in everyday life [1,2]. The concept of a Li-ion battery was proposed by SONY in 1990 following their first use with $LiCoO_2$ and graphite electrodes [3]. Since then, Li-ion batteries have been studied to satisfy the increasing energy demands for portable electronic devices [4]. Recently, energy and environmental challenges to stimulate research for hybrid electric vehicles instead of cars have emerged. Hence, Li-ion batteries with high energy density, high power density, low cost, and environmental friendliness have become prominent

[5,6]. Li-rich layered solid solution cathode materials such as $y\mathrm{Li_2MnO_3}\cdot(1\text{-}y)\mathrm{LiMO_2}$ ($0 < y < 1$, M = Ni, Co, Mn, Fe, $\mathrm{Ni}_x\mathrm{Mn}_{1\text{-}x}$, $\mathrm{Ni_{1/3}Mn_{1/3}Co_{1/3}}$), that not only exhibit high practical capacity, but also demonstrate an initial charging voltage of more than 4.5 V and discharge capacity of up to 200 $\mathrm{mAh\cdot g^{-1}}$, have received extensive attention [7-10]. Furthermore, the discharge capacity of some lithium-rich layered oxides can be as high as 300 $\mathrm{mAh\cdot g^{-1}}$, which is almost twice as high as that of commercial cathode materials [11]. Additionally, the component $\mathrm{Li_2MnO_3}$ evolves to $\mathrm{MnO_2}$ with electrochemical activity after the initial charge when the charging voltage exceeds 4.5 V and subsequently changes into $\mathrm{LiMnO_2}$ when discharging; meanwhile, Mn is in high-spin states of $\mathrm{Mn^{3+}}$ [12,13] and promotes the activation of $\mathrm{Li_2MnO_3}$. This confers the different electrochemical characteristics of lithium-layered lithium batteries, which are obtained by adjusting the content of $\mathrm{LiMO_2}$ and $\mathrm{Li_2MnO_3}$ of the lithium-rich layered cathode material. Many studies have focused on the influence of Ni and Mn on the structure and electrochemical properties of lithium-rich materials[14,15]. As is known, Ni exhibits poor thermal stability but can provide high capacity, while Mn can stabilize the structure and safety of the material [16]. The crystalline structure of $x\mathrm{Li_2MnO_3}\cdot(1\text{-}x)\mathrm{LiMO_2}$ can change easily from the layered to the spinel phase, thus resulting in capacity attenuation and voltage decay [17]. Due to the different ratios of nickel and manganese in $x\mathrm{Li_2MnO_3}\cdot(1\text{-}x)\mathrm{LiMO_2}$, the materials have different energy densities. There is no detailed study on this cause. We consider it necessary to study whether the capacity of lithium-rich materials primarily depends on $\mathrm{Ni^{2+/3+}}$, $\mathrm{Ni^{3+4+}}$, or $\mathrm{Mn^{3+/4+}}$ and what are the roles of $\mathrm{Ni^{2+/3+}}$, $\mathrm{Ni^{3+4+}}$ and $\mathrm{Mn^{3+/4+}}$, to obtain clear insights for high-performance lithium-rich materials.

In this study, we synthesized a series of lithium-rich materials with the molecular formula $\mathrm{LiNi}_x\mathrm{Mn}_{1\text{-}x}\mathrm{O_2}\cdot\mathrm{Li_2MnO_3}$ (x = 0.6, 0.7, 0.8, 0.9, 1) from an $\mathrm{Ni}_x\mathrm{Mn}_{1\text{-}x}(\mathrm{CO_3})_2$ (x = 0.6, 0.7, 0.8, 0.9, 1) precursor to study the effect of $\mathrm{Ni^{2+/3+}}$, $\mathrm{Ni^{3+4+}}$, and $\mathrm{Mn^{3+/4+}}$ on the electrochemical properties for Li-rich materials. The relationship among the cathode materials of different Ni–Mn ratios and their electrochemical performances were elucidated by their lattice structure, morphologies, cycle and rate performances, X-ray photoelectron spectroscopy, and electrochemical impedance spectroscopy tests. For electrochemical performance testing, all cells were activated at 40 $\mathrm{mA\cdot g^{-1}}$ for the first five cycles and subsequently charged/discharged at different current densities from 20 $\mathrm{mA\cdot g^{-1}}$ to 160 $\mathrm{mA\cdot g^{-1}}$.

2. EXPERIMENTAL

2.1. Synthesis of spherical materials

Precursors with chemical formulas of the form $\mathrm{Ni}_x\mathrm{Mn}_{1\text{-}x}(\mathrm{CO_3})_2$ (x = 0.6, 0.7, 0.8, 0.9, 1) were fabricated by carbonate co-precipitation. During preparation, manganese sulfate monohydrate and nickel sulfate hexahydrate were used as the Mn and Ni sources, respectively; sodium carbonate as the precipitant to subside the metallic ions; and ammonium hydroxide as the chelating agent to combine Ni and Mn divalent ions to form stable chelates, thereby ensuring the homogeneous growth of the precursor. $\mathrm{MnSO_4\cdot H_2O}$ and $\mathrm{NiSO_4\cdot 6H_2O}$ were dissolved in deionized water in a mixed concentration of 2 $\mathrm{mol\cdot L^{-1}}$, while the concentrations of $\mathrm{NH_3\cdot H_2O}$ and $\mathrm{Na_2CO_3}$ were 0.3 $\mathrm{mol\cdot L^{-1}}$ and 1 $\mathrm{mol\cdot L^{-1}}$, respectively. The mixed solution of $\mathrm{MnSO_4\cdot H_2O}$ and $\mathrm{NiSO_4\cdot 6H_2O}$ as well as that of $\mathrm{Na_2CO_3}$ and $\mathrm{NH_3\cdot H_2O}$ were injected simultaneously into a stirred reactor dropwise. The pH in the container remained at approximately 7.8, and the bath temperature was 55 °C; the mixture was stirred vigorously at 800 r/min in a continuous stirred-tank reactor for 10 h. The resulting precipitates were collected and washed four times to remove residual sodium and sulfate radicals, and subsequently dried at 80 °C for 12 h. The obtained precursors were mixed uniformly with Li_2CO_3 according to a predetermined stoichiometry, and subsequently pre-sintered at 550 °C for 5 h and sintered at 800 °C for 10 h in a muffle furnace. The technological composition for each metal in $LiNi_xMn_{1-x}O_2{\cdot}Li_2MnO_3$ for $x = 0.6$, 0.7, 0.8, 0.9 and 1 is the same as the stoichiometry determined by inductively coupled plasma (ICP) spectroscopy. The resulting products $LiNi_xMn_{1-x}O_2{\cdot}Li_2MnO_3$ (LNMs) for $x = 0.6$, 0.7, 0.8, 0.9 and 1 are marked as LNM64, LNM73, LNM82, LNM91, LNM10, respectively for short.

2.2. Structure and electrochemical characterization

The crystal structure of the material was characterized in the 2θ range of 10–120° with a step size of 0.02° by powder X-ray diffraction (XRD, D/Max2500PC, Japan) using Cu Kα radiation, a graphite monochromator, and tube voltage and tube current of 30 kV and 100 mA, respectively. Scanning electron microscopy (SEM, Nova Nano SEM 450, America) was performed to identify the morphology and microstructure of the products. An electrochemical workstation (Zahner Elektrik IM6, Germany) was used to obtain the electrochemical impedance spectrum in the frequency range from 100 mHz to 100 kHz with an amplitude of 5 mV.

The prepared powder, acetylene black, and polyvinylidene fluoride were blended into the slurry according to the weight ratio of 80:8:12, and then applied evenly onto an aluminum foil. Subsequently, the foil was cut into round pieces of diameter 11 mm, after being dried at 120 °C for 12 h. CR2016 coin-type cells were fabricated in a glove box filled with argon. A metallic lithium plate was used as the anode, Cellgard2400 porous polypropylene films were used as the separator, and the electrolyte was 1 M $LiPF_6$ solution in EC:DEC:EMC with a volume ratio of 1:1:1. The charge and discharge tests of all cells were performed at room temperature at 40 $mA{\cdot}g^{-1}$ initially, and subsequently at different current densities (20–160 $mA{\cdot}g^{-1}$) with the LAND CT2001A battery test system, in which the test voltage range was 2–5 V. The dV/dQ curve analysis is obtained from the differentiation of the charge/discharge curve (voltage–capacity curve).

3. RESULTS AND DISCUSSION

The XRD patterns of the final products are depicted in Fig. 1. The XRD patterns of all samples exhibit high crystallinity, and the structures agree well with the α-$NaFeO_2$ layered structure of the R-3m space group and Li_2MnO_3 of the C2/m space group. Clear characteristic peaks of Li_2MnO_3 are visible in the magnified image of the diffraction peak between 20 and 25° in all samples; these characteristic peaks are attributed to the superlattice arrangement of Li^+ in the transition metal layer. The splitting peaks (006)/(102) and (018)/(110) are independent and the splitting degree is obvious, indicating the typical layered structure of the final samples.

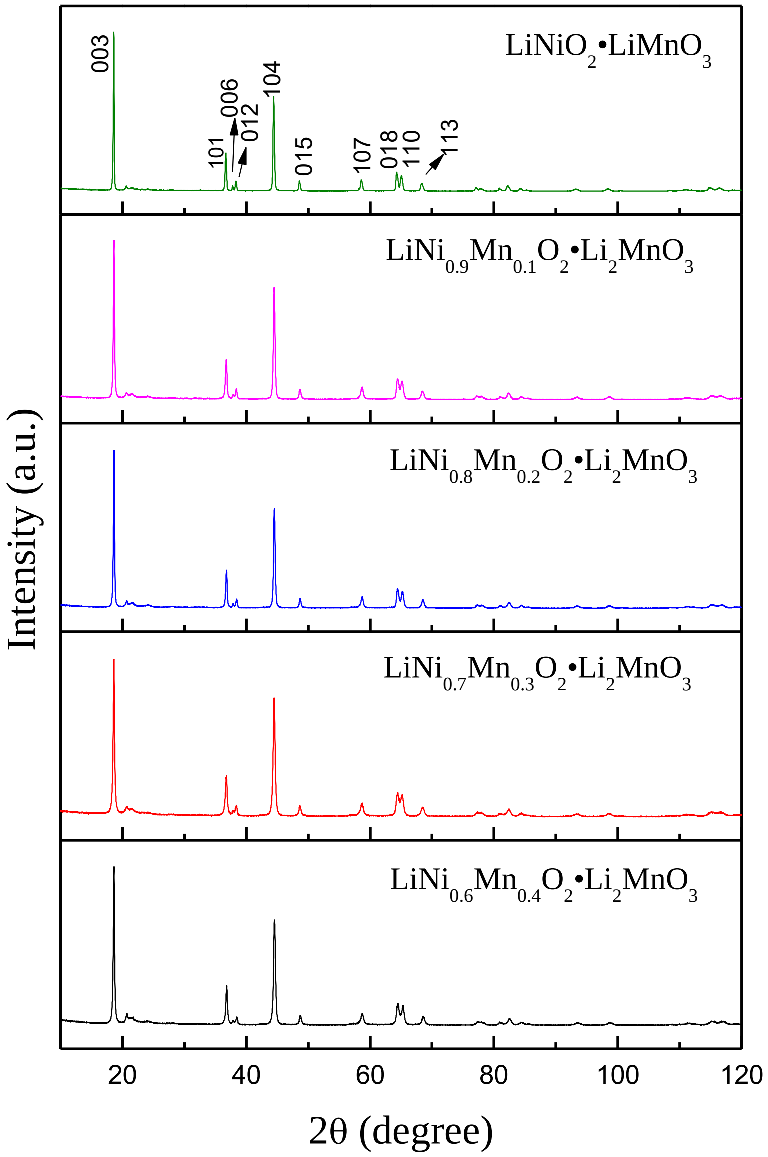

Figure 1. XRD patterns of LNMs.

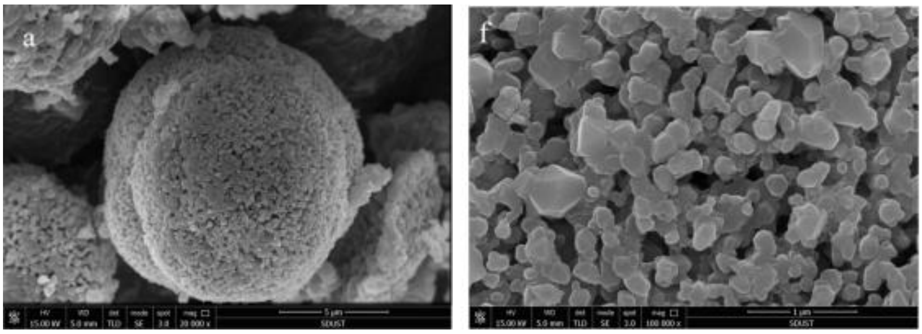

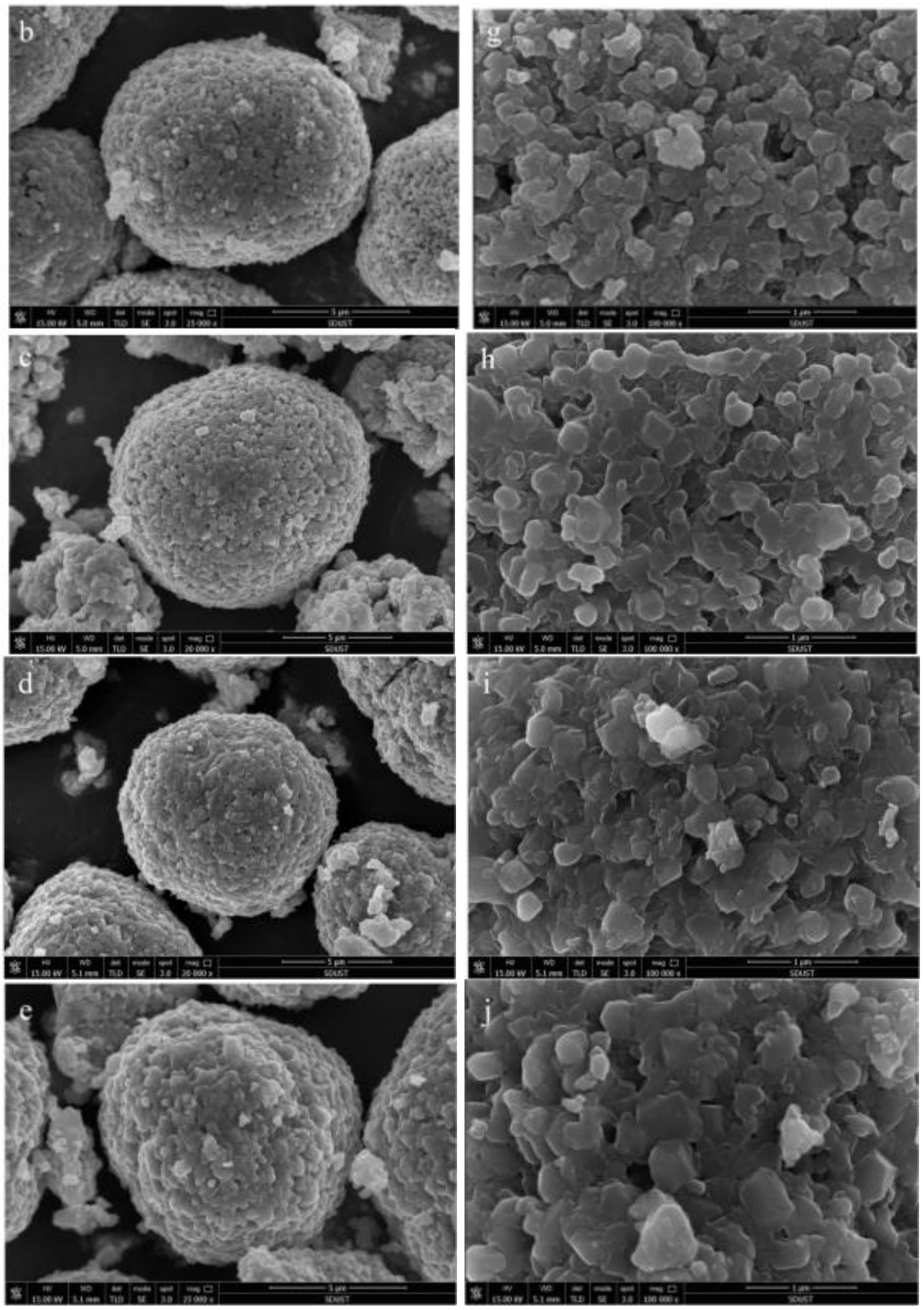

Figure 2. SEM images of (a, f) LNM64, (b, g) LNM73, (c, h) LNM82, (d, i) LNM91, (e, j) LNM10.

SEM images of LNMs are presented in Fig. 2. As shown, all final products are composed of spherical particles with high sphericity and dispersion. Meanwhile, the images in Fig. 2f–j indicate that the secondary particles are aggregates formed by nanostructured primary particles that grow larger with the increase in Ni/Mn ratio. Additionally, as the Ni/Mn ratio increases, the particles agglomerate, and clearly. The smaller primary particles is beneficial to the intercalation/deintercalation of Li^+ during charge/discharge. The result is consistent with that of previous literature [18]. In conclusion, the ratio of Ni/Mn can change the size of the primary particles and the tap density of the secondary particles.

Fig. 3a shows the fitting results of the XPS spectra of Ni2p for LNMs; the binding energies and cation distributions for Ni^{2+} and Ni^{3+} are shown in Table 1. The reported Ni2p XPS BEs (Binding

Energies) of Ni^{2+} and Ni^{3+} are located at 853.7–855 eV and 855.3–855.9 eV, respectively [19, 20]. As shown in Table 1, the valence states of the Ni ions are 2+ and 3+ in all samples, and Ni^{2+} accounts for a larger proportion. Additionally, the content of Ni^{2+} decreases gradually from 65.21% to 47.73%, while the content of Ni^{3+} increases gradually from 34.79% to 52.27%. The result is calculated by multiplying the proportion of Ni in the molecular formula of the transition metal by the percentage of Ni^{2+} in the XPS analysis. An example is the calculation process for sample LNM64, which is (0.6/2)*0.6521. The content of divalent Ni increases first until the maximum value when Ni content is 0.9 and then decreases with higher Ni content. The Mn spectra are presented in Fig. 3b, the reported Mn2p XPS BEs of Mn^{4+} are located at 641.4–644.8 eV, and the data in Table 1 show that the valence states of Mn in the samples are all +4.

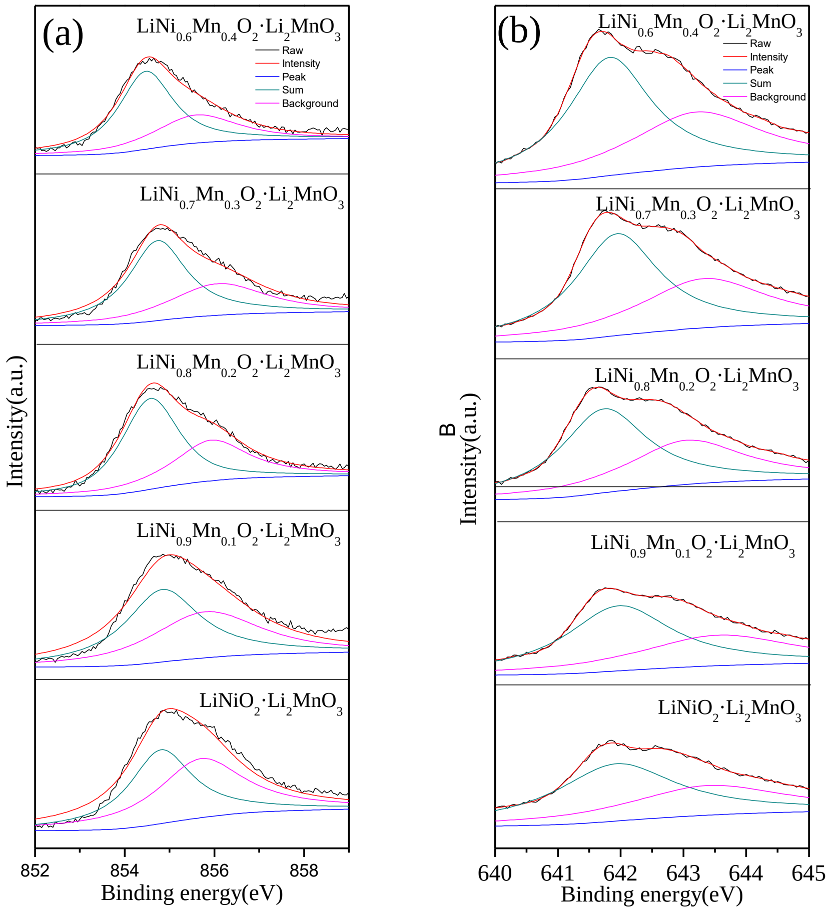

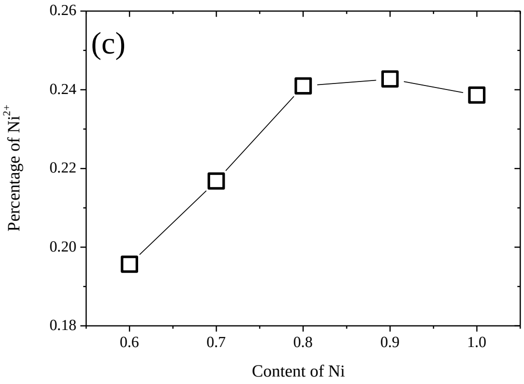

Figure 3. XPS spectra of (a) Ni2p and (b) Mn2p for LNMs and (c) the percentage of Ni^{2+} participating in discharge during discharge.

Table 1. Binding energy and cation distribution of Ni2p and Mn2p from XPS of LNMs

Sample	Binding energy (eV)				Cation distribution (%)	
	Ni^{2+}	Ni^{3+}	Mn^{4+}	Mn^{4+}	Ni^{2+}	Ni^{3+}
$LiNi_{0.6}Mn_{0.4}O_2 \cdot Li_2MnO_3$	854.47	855.59	641.82	643.20	65.21	34.79
$LiNi_{0.7}Mn_{0.3}O_2 \cdot Li_2MnO_3$	854.74	856.07	641.94	643.33	61.94	38.06
$LiNi_{0.8}Mn_{0.2}O_2 \cdot Li_2MnO_3$	854.57	855.92	641.83	643.03	60.24	39.76
$LiNi_{0.9}Mn_{0.1}O_2 \cdot Li_2MnO_3$	854.86	855.8	641.97	643.55	53.94	46.06
$LiNiO_2 \cdot Li_2MnO_3$	854.80	855.7	641.93	643.39	47.73	52.27

Fig. 4 presents discharge capacity of the of LNMs cathodes at different current density. The initial discharge capacity of LNMs increases firstly to reach a maximum of 217.7 mAh g^{-1} for LNM82 and subsequently decreases with increasing Ni content. As is known, a high crystallinity and well-formed structure can enhance the structural stability of materials during cycling. A small primary particle size can increase the specific surface area, and a shorter diffusion distance of Li ions as well as the reversible capacity, thereby resulting in excellent rate performance [21]. Further, the Li_2MnO_3 component can stabilize the structure of the material, and the $LiNi_xMn_{1-x}O_2$ component is electrochemically active below 4.5 V, thus mainly contributing to the capacity [22]. As shown in Fig. 4, the rate capabilities of all samples improve and then deteriorate with the increase in the Ni/Mn ratio. The LNM82 sample has the highest discharge capacities of approximately 242 mAh·g^{-1} (20 mA·g^{-1}), 225 mAh·g^{-1} (40 mA·g^{-1}), 215 mAh·g^{-1} (80 mA·g^{-1}), and 188 mAh·g^{-1} (160 mA·g^{-1}) at all current densities.

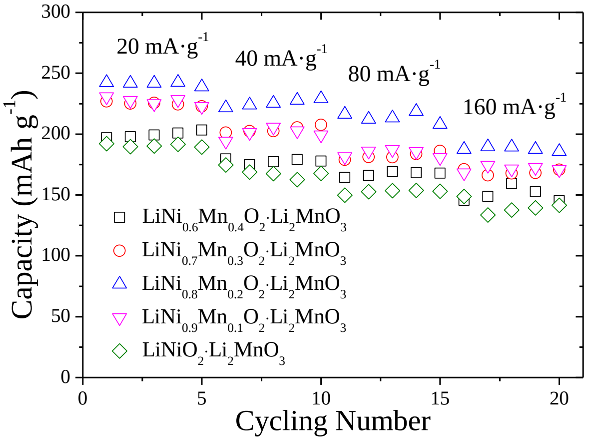

Figure 4. Cycling and rate performances of LNMs at room temperature at different current density values during 2.0–5.0 V.

To get insight into the electrochemical reaction, dQ/dV curves for the cathode materials in the first five cycles at 40 mA·g^{-1} are plotted, as displayed in Fig. 5. The charging curves for the first cycle of all samples differ significantly from those of the following cycles. The peak at approximately 4.8 V is related to the activation of Li_2MnO_3 and this process is irreversible for of Li^+ extraction and the loss of O^{2-}[23]. Moreover, it is obvious that the peak of LNM82 is the strongest, thereby implying that the fullest activation of Li_2MnO_3 components and the content of Li_2MnO_3 affect the peak significantly [24]. This result is consistent with the initial charge/discharge data. The peak of 4.1 V is attributed to the oxidation reaction of $Ni^{2+/}Ni^{3+/}Ni^{4+}$ and evolves to 3.8 V oxidation peaks ($Ni^{2+/}Ni^{3+}$) and 4.45 V oxidation peaks ($Ni^{3+/}Ni^{4+}$) in the next few cycles. The corresponding reduction peaks are located at approximately 3.7 V ($Ni^{3+/}Ni^{2+}$) and 4.35 V ($Ni^{4+/}Ni^{3+}$) [25]. A new pair of redox peaks appears at approximately 3.5 V/3.3 V, that corresponds to the reaction of $Mn^{4+/}Mn^{3+}$ derived from MnO_2 generated after the activation of Li_2MnO_3[26]. Further, the peak near 3.3 V shifts to a lower voltage range, indicating the gradual transformation from the layered structure to spinel phase during the following cycles [27]. Because the intercalation/deintercalation of lithium ions in MnO_2 is reversible, the dQ/dV curves for the following few cycles are highly similar.

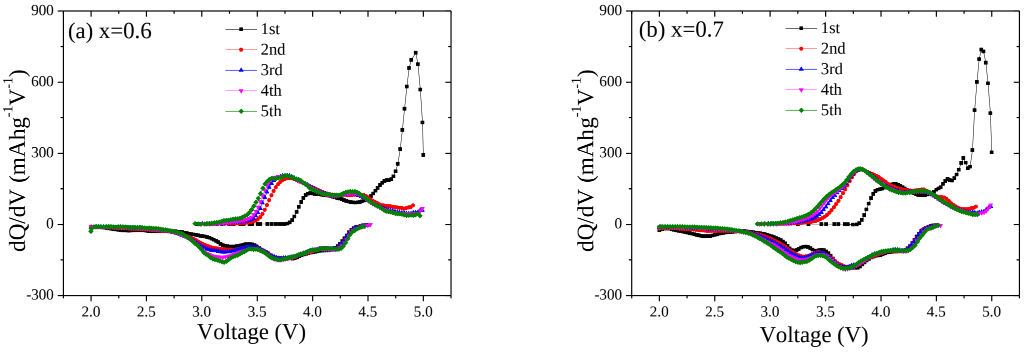

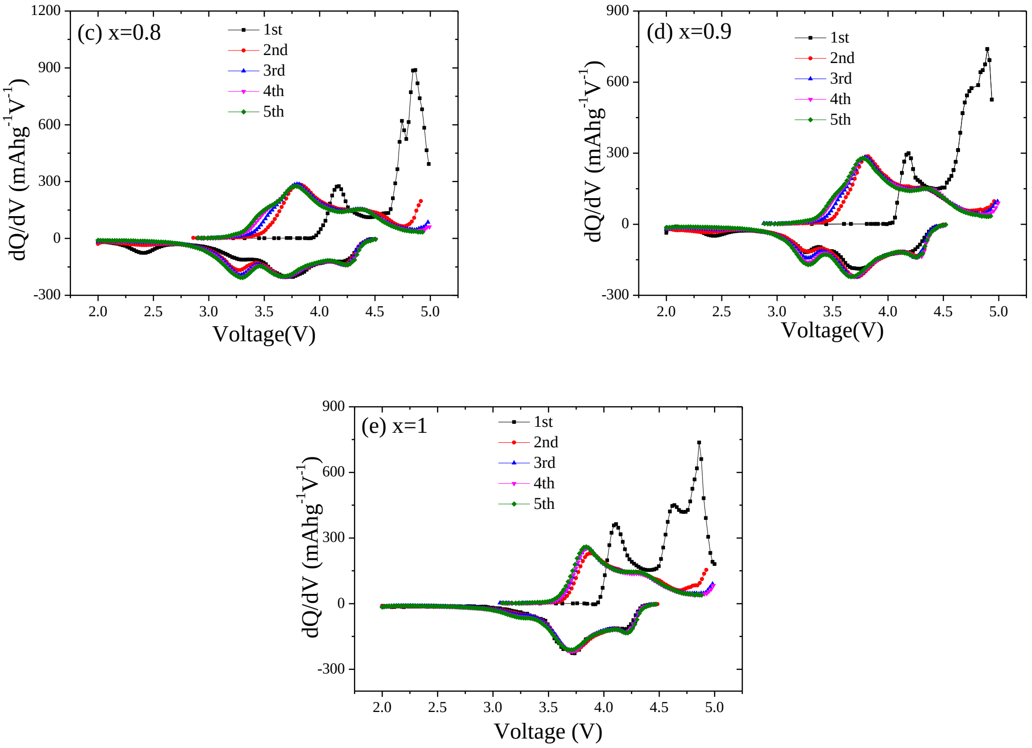

Figure 5. dQ/dV curves of (a) LNM64, (b) LNM73, (c) LNM82, (d) LNM91, (e) LNM10 in the first five cycles at 40 mA·g^{-1}.

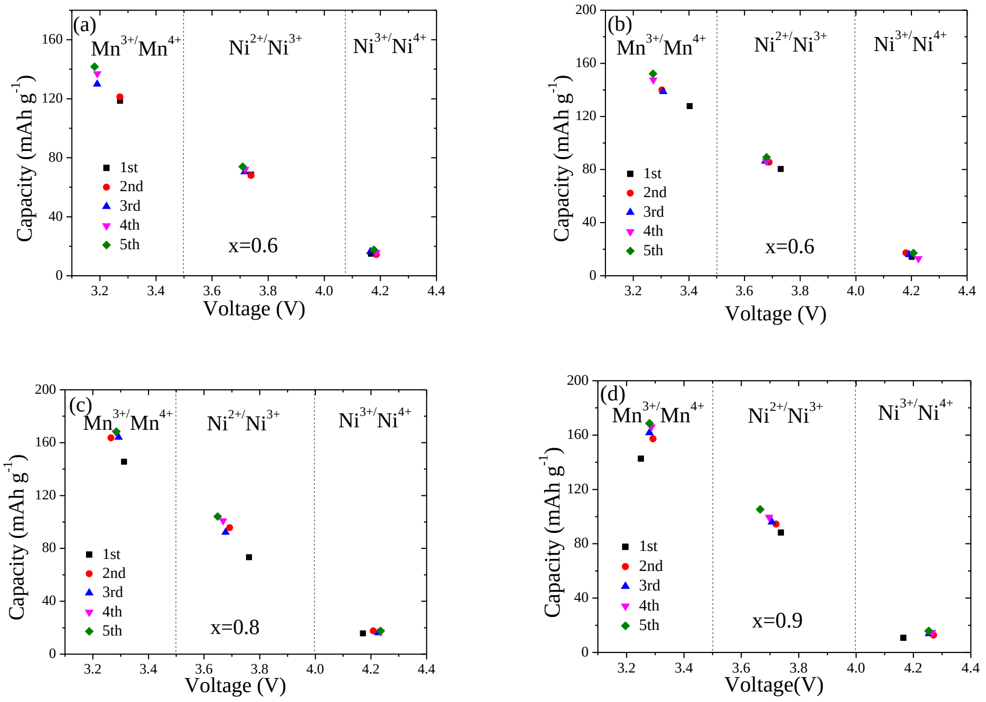

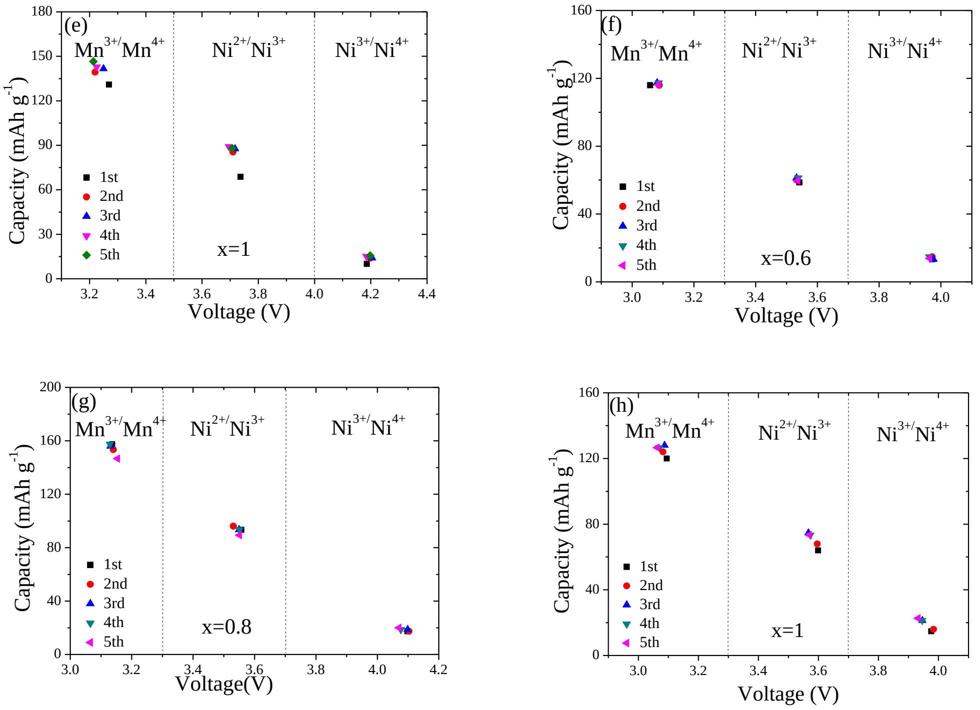

Figure 6. Change in voltage and capacity corresponding to the reduction of $Ni^{2+/}Ni^{3+}$, $Ni^{3+/}Ni^{4+}$, and $Mn^{3+/}Mn^{4+}$ in the first five cycles of (a) LNM64, (b) LNM73, (c) LNM82, (d) LNM91, (e) LNM10 at 40 mA·g^{-1}, corresponding to the reduction of $Ni^{2+/}Ni^{3+}$, $Ni^{3+/}Ni^{4+}$, and $Mn^{3+/}Mn^{4+}$ with the number of cycles of (f) LNM64, (g) LNM82, (h) LNM10 at 80 mA·g^{-1}.

Fig. 6a–e displays the change in the voltage and capacity corresponding to the reduction peaks of $Ni^{2+/}Ni^{3+}$, $Ni^{3+/}Ni^{4+}$, and $Mn^{3+/}Mn^{4+}$ in the first five cycles of LNMs at room temperature under 40 mA·g^{-1}. The capacity associated with the reduction in $Mn^{3+/}Mn^{4+}$ for all samples increases gradually with the number of cycles. This is because the Li_2MnO_3 components are activated gradually during the charge process of the first few cycles to provide more Mn^{3+} to participate in the reaction during the discharge process, and ultimately provide higher capacity. The capacity corresponding to the reduction peak of $Ni^{2+/}Ni^{3+}$ is also shown as an increase in the number of cycles in general. However, the voltage corresponding to the reduction peak of $Ni^{2+/}Ni^{3+}$ and $Mn^{3+/}Mn^{4+}$ exhibits a decayingtrend with increasing cycles and current density, while the voltage corresponding to the reduction peak of $Ni^{3+/}Ni^{4+}$ is in the stable state. The median voltage attenuation shown in Fig. 7 can also be used as an evidence for voltage decay. Additionally, the changes in capacity and voltage corresponding to the reduction peak of $Mn^{3+/}Mn^{4+}$ and $Ni^{2+/}Ni^{3+}$ are more obvious than that of $Ni^{3+/}Ni^{4+}$. As shown in Fig. 6f–h, the change in voltage and capacity for all reduction peaks is smaller at a current density of 80 mA·g^{-1} compared to when the current is 40 mA·g^{-1}.

The electrochemical impedance spectroscopic measurements of the as-prepared samples of LNMs were performed after five cycles at room temperature at 40 mA·g^{-1}, as shown in Fig. 8. The equivalent circuit is $R_1(C_1R_2)(C_2R_3)W$ and the fitting results are in good agreement with the experimental data. R_1 represents the Ohmic impedance (R_e) in the high-frequency region. R_2 represents the interfacial layer resistance (R_{sf}) that is a semicircle in the high-frequency region shown in the figure, while R_3 represents the charge transfer resistance (R_{ct}) that is a larger semicircle in the relatively low frequency region. The slope in the low-frequency region is related to Li^+ diffusion in the bulk materials [28, 29]. For a more intuitive understanding of the impedances of each sample, the resistance fitting results and Warburg factor (σ) are given in Table 2. Charge transfer is easier to perform for the LNM82, thus leading to a smaller value of R_{ct} (13.08 Ω) and hence excellent electrochemical properties. However, LNM10 presents the highest R_{ct} of 25.48 Ω, indicating that the efficiency of insertion/extraction for Li^+ is inhibited and hence poor electrochemical properties.

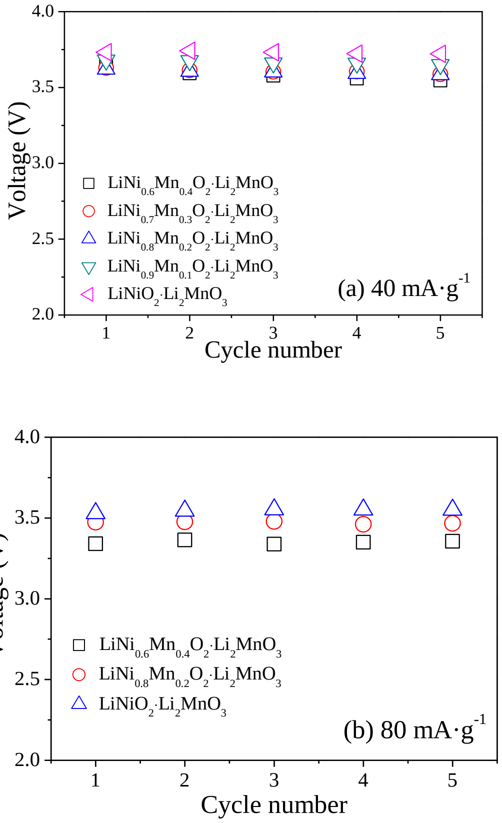

Figure 7. The median voltage of discharge in the first five cycles of LNMs at (a) 40 $mA·g^{-1}$ and (b) 80 $mA·g^{-1}$.

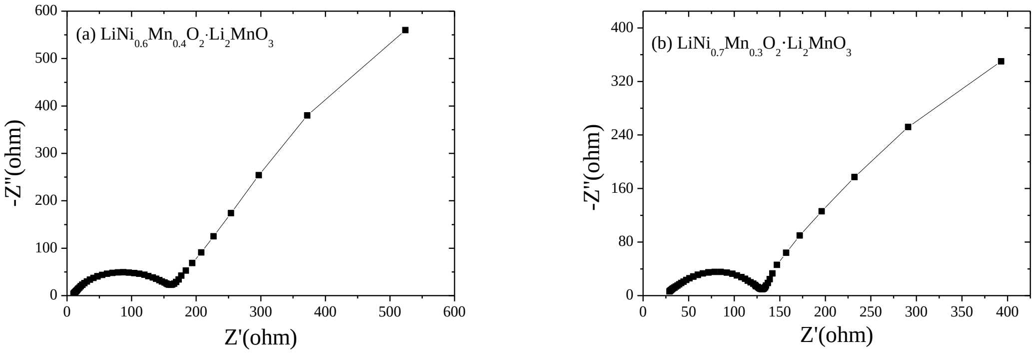

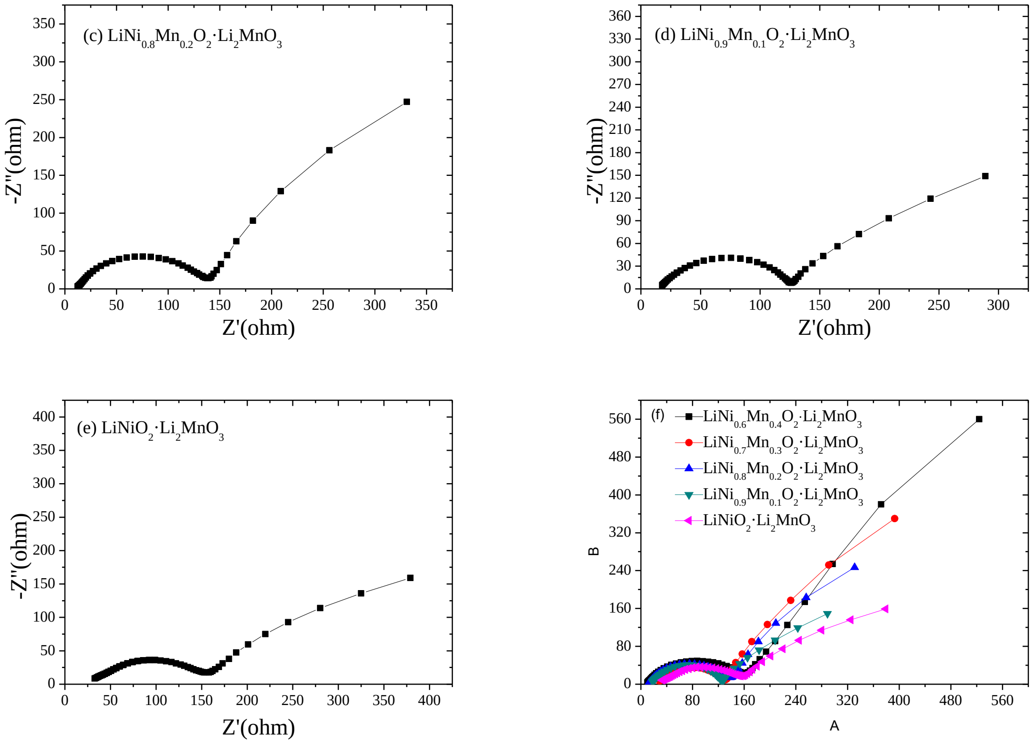

Figure 8. AC impedance spectra of LNMs after five cycles at room temperature at 40 mA·g^{-1}.

Table 2. Resistance fitting results

Sample	Re (Ohm)	Rsf (Ohm)	Rct (Ohm)	σ (ΩHz$^{1/2}$)
$LiNi_{0.6}Mn_{0.4}O_2 \cdot Li_2MnO_3$	10.41	98.46	17.68	352.24779
$LiNi_{0.7}Mn_{0.3}O_2 \cdot Li_2MnO_3$	28.29	67.58	17.34	263.11547
$LiNi_{0.8}Mn_{0.2}O_2 \cdot Li_2MnO_3$	13.04	89.35	13.08	198.13306
$LiNi_{0.9}Mn_{0.1}O_2 \cdot Li_2MnO_3$	17.7	81.47	15.81	148.15455
$LiNiO_2 \cdot Li_2MnO_3$	32.92	78.99	25.48	190.15023

The redox reaction process of the Ni^{2+}/Ni^{3+} redox pair provides most of the capacity of LNMs during the discharge process compared to the discharge capacity provided by Ni^{3+}/Ni^{4+} and Mn^{3+}/Mn^{4+}. Additionally, the capacity provided by the reduction reaction of Ni^{3+}/Ni^{4+} is almost unaffected by the composition of the samples. Fig. 9 shows the variation in capacity according to the Ni and Mn contents at a current of 20 mA·g^{-1} after five cycles that are obtained by peaking the dQ/dV reduction peak. The total discharge capacity provided by the reduction reaction of Ni^{2+}/Ni^{3+} and Ni^{3+}/Ni^{4+} first increased from 103.2 mAh·g^{-1} for LNM64 to the maximum value of 144.6 mAh·g^{-1} for LNM91, and subsequently decreased to 139.9 mAh·g^{-1} for LNM10 with the increase in Ni content.

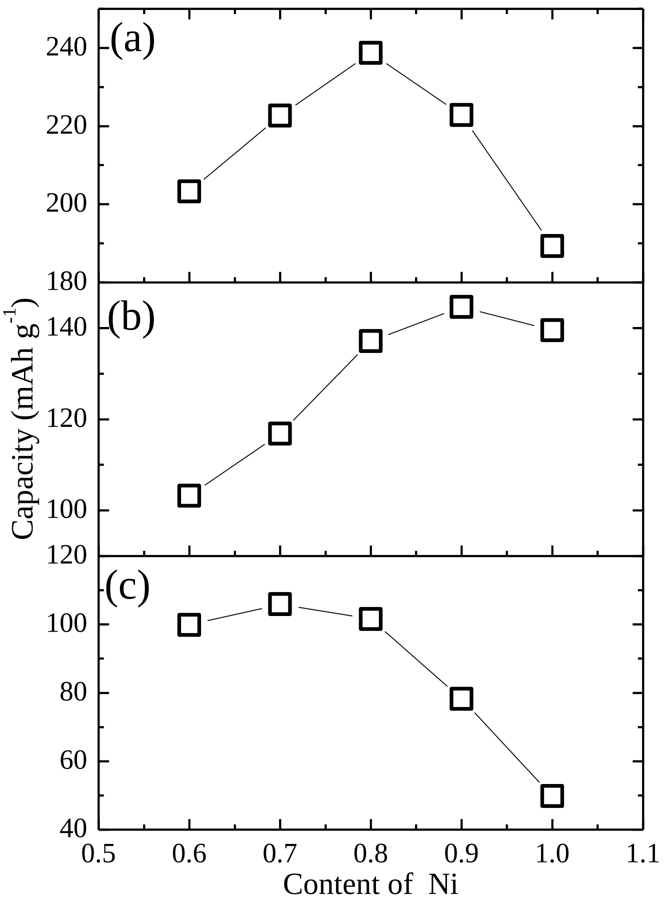

Figure 9. (a) The discharge capacity and discharge capacity trends provided by the reduction reaction of (b) Ni^{2+}/Ni^{3+} and Ni^{3+}/Ni^{4+}, (c) Mn^{3+}/Mn^{4+} after five cycles of LNMs samples at 20 mA·g^{-1}.

The Ni content in the samples increased gradually while the percentage of Ni^{2+} decreased gradually; their combined effect on the discharge capacity caused the total discharge capacity provided by the reduction reaction of Ni^{2+}/Ni^{3+} and Ni^{3+}/Ni^{4+} in Fig. 9b to first increase and subsequently decrease. Fig. 9b clearly shows that the amount of Ni^{2+} involved in the discharge process is consistent with the results obtained in Fig. 3d. Meanwhile, the discharge capacity corresponding to the reduction reaction of Mn^{3+}/Mn^{4+} first increased from 99.8 mAh·g^{-1} for LNM64 to 105.9 mAh·g^{-1} for LNM73, and subsequently decreased to 49.4 mAh·g^{-1} for sample LNM91 with the decrease in Mn content in the samples, as shown in Fig. 9c. The discharge capacity of the material decreases with the decrease in Mn content. This is due to the lack of Mn^{4+} in the $LiNiO_2$ component of the LNMs sample [22]. However, the transition metal doping in Li_2MnO_3 increases the discharge capacity [30]; therefore, the capacity will first increase and then decreases, as shown in Fig. 9c. In addition, the discharge capacity decreases with the decrease in Mn content and increases with the increase in Ni content, owing to the influence of Ni ions on Mn ions. Fig. 9a clearly shows the upward trend of the discharge capacity in the beginning. In summary, the LNM82 delivers the highest discharge capacity under all rates owing to the co-influences of Ni^{2+}/Ni^{3+}, Ni^{3+}/Ni^{4+}, and Mn^{3+}/Mn^{4+}, in which the influence of Ni^{2+}/Ni^{3+} is the primary factor.

4. CONCLUSIONS

In this study, spherical Li-rich layered nanostructured materials of LNMs were synthesized by carbonate co-precipitation, and the effects of $Ni^{2+/}Ni^{3+}$, $Ni^{3+/}Ni^{4+}$, and $Mn^{3+/}Mn^{4+}$ on the electrochemical properties of the Li-rich cathode materials were studied. As the Ni content increased, the discharge capacity of LNMs first increased to that of LNM82 and subsequently decreased at all rates. This phenomenon was associated with the total capacity provided by the reduction reactions of $Ni^{2+/}Ni^{3+}$ and $Ni^{3+/}Ni^{4+}$, that first increased to LNM91 and subsequently decreased, while the capacity provided by the reduction reaction of $Mn^{3+/}Mn^{4+}$ first increased to that of LNM73 and subsequently decreased. The presence of $Ni^{2+/}Ni^{3+}$ contributed significantly to the capacity of LNMs compared to $Ni^{3+/}Ni^{4+}$ and $Mn^{3+/}Mn^{4+}$, and the composition of the samples exhibited little effect on the capacity provided by $Ni^{3+/}Ni^{4+}$ during reduction. From the EIS, the variation trend of the lithium ion diffusion coefficient coincided with that of the discharge capacity resulting from the reduction reaction of $Ni^{2+/}Ni^{3+}$. In addition, LNM82 exhibited the smallest R_{ct} and hence the maximum discharge capacity. We believe that through the research of this project, we can provide guidance on how to provide a suitable ratio of Ni and Mn to obtain high-performance lithium-rich materials.

ACKNOWLEDGEMENTS
This work was financially supported by National Natural Science Foundation of China (No. 51641206), Shandong Natural Science Foundation Project (No. ZR2015EM013) and special funds for independent innovation and transformation of achievements in Shandong Province (Grant No. 2014CGZH0911).

References

1. B. Scrosati and J. Garche, *J. Power Sources,* 195 (2010) 2419.
2. J.Q. Xu, H.R. Thomas, R.W. Francis, K.R. Lum, J.W. Wang and B. Liang, *J. Power Sources*, 177 (2008) 512.
3. W.K. Pang, C.Z. Lu, C.E. Liu, V.K. Peterson，H.F. Lin，S.C. Liao and J.M. Chen, *J. Phys. Chem. Chem. Phys.,* 18 (2016) 17183.
4. R. Santhanam and B. Rambabu, *J. Power Sources*, 195 (2010) 5442.
5. Y.Y. Sun, F. Li, Q.Q. Qiao, J.S.Cao, Y.L. Wang and S.H. Ye, *Electrochim. Acta*, 176 (2015) 1464.
6. Q.X. Ma, R.H. Li, R.J. Zheng, Y.L. Liu, H. Huo and C.S. Dai, *J. Power Sources*, 331 (2016) 112.
7. Y. Bai, Y. Li, C. Wu, J, Lu. H. Li, Z. Liu, Y. Zhong, S. Chen, C. Zhang, K. Amine and F. Wu, *Energy Technology*, 3 (2015) 843.
8. A. Watanabe, K. Yamamoto, T. Uchiyama, T. Matsunaga, A. Hayashi, K. Maeda, H. Kageyama and Y. Uchimoto, *ACS Appl. Energy Mater.*, 3 (2020) 4162.
9. M. Gao, L. Fang, H.Q. Liu, C.J. Tian, L.L. Ma and W.Y. Yang, *Electrochim. Acta*, 95 (2013) 87.
10. M. Wang, L. Chen, M. Liu, Y. Chen and Y. Gu, *J. Alloys Compd.*, 848 (2020) 156620.
11. H. Yu and H. Zhou, *J. Phys. Chem. Lett.*, 4 (2013) 1268.
12. J. Meng, B. Key, Y.S. Meng and C.P. Grey, *Chem. Mater.*, 21 (2009) 2733.
13. J.L. Liu, J. Wang and Y.Y. Xia, *Electrochim. Acta*, 56 (2011) 7392.
14. M. Kasai, H. Dohi and S. Nishimura, *Solid State Ionics*, 289 (2016) 77.
15. H. Konishi, T. Hirano, D. Takamatsu, A. Gunji, X.L. Feng, S. Furutsuki, T. Okumura and S. Terada, *Solid State Ionics*, 308 (2017) 84.
16. H.J. Noh, S. Youn, S.Y. Chong and Y.K. Sun, *J. Power Sources*, 233 (2013) 121.

17. P. Yan, A. Nie, J. Zheng, Y. Zhou, D. Lu, X. Zhang, R. Xu, I. Belharouak, X. Zu, J. Xiao, K. Amine, J. Liu, F. Gao, R. Shahbazian-Yassar, J. Zhang, and C. Wang .*J. Nano Lett*., 15 (2015) 514.
18. J.H. Liu, H.G. Chen , J.N. Xie, Z.Q. Sun, N.N. Wu and B.R. Wu, *J. Power Sources*, 251 (2014) 208.
19. S.K. Chong, Y.N. Liu, W.W. Yan and Y.Z. Chen, *Rsc Adv*., 6 (2016) 53662.
20. M. Zubair, G. Li, B. Wang, L. Wang and H. Yu, *ACS Appl. Energy Mater*. 2 (2019) 503.
21. F. Yang, Q.G. Zhang, X.H. Hu and T.Y. Peng, *Electrochim. Acta*, 165 (2015) 182.
22. F. Yang, Q.G. Zhang, X.H. Hu, T.Y. Peng and J.Q. Liu, *J. Power Sources*, 353 (2017) 323.
23. H.Q. Liu, Q. Su, C.H. Yuan, T. Yuan, Y.J. Gu and H.Z. Cui, J. Appl. Electrochem., 47 (2017) 1.
24. M. Kasai, H. Dohi and S. Nishimura, *Solid State Ionics*, 289 (2016) 77.
25. J.X. Huang, B. Li, B. Liu, J.B. Zhao and B. Ren, *J. Power Sources*, 310 (2016) 85.
26. X.D. Xiang and W.S. Li, *Electrochim. Acta*, 127 (2014) 259.
27. T. Yuan, H.Q. Liu, Y.J. Gu, H.Z. Cui and Y.M. Wang, *Appl. Phys.* A, 122 (2016) 812.
28. Y.J. Gu, Y. Li, Y. Fu, Q.F. Zang, H.Q. Liu, J.X. Ding, Y.M. Wang and J.F. Ni, *Electrochim. Acta*, 176 (2015) 1029.
29. B. Huang, M. Wang, X. Yang, G. Xu and Y. Gu, *J. Alloys Compd*., 808 (2019) 151683.
30. Z.Q. Wang, M.S. Wu, B. Xu and C.Y. Ouyang, *J. Alloys Compd*., 658 (2016) 818.